

$P_4W_{20}O_{68}$: A complex charge-density-wave modulated structure with an antiferroelectric-like lattice distortion

P. Roussel,* Ph. Labbé, H. Leligny, and D. Groult

Laboratoire CRISMAT, CNRS UMR 6508, ISMRA—Université de Caen, 14050 Caen Cédex, France

P. Foury-Leylekian and J. P. Pouget

Laboratoire de Physique des Solides, CNRS UMR 8502, Université de Paris Sud, 91405 Orsay Cédex, France

(Received 29 July 1999)

The charge-density-wave (CDW) structure of the monophosphate tungsten bronze $P_4W_{20}O_{68}$, the $m=10$ member of the $(PO_2)_4(WO_3)_{2m}$ series has been solved at room temperature from single-crystal x-ray-diffraction data. In agreement with previous x-ray diffuse scattering experiments, intense first-order satellite reflections at $\pm \frac{3}{7}\mathbf{a}^*$ reduced wave vectors as well as second-order satellite reflections at $\pm \frac{1}{7}\mathbf{a}^*$ were observed. The CDW structure was refined in a four-dimensional (4D) formalism and found to have the superspace group $P2_1(\alpha 00)0$. The modulation, of the displacive type, involves mainly the tungsten atoms inside the different WO_6 octahedra of the WO_3 -type slab. The W displacements, which are mostly oriented in the direction of the segment of 10 WO_6 octahedra building the slab, tends to be oriented in opposite directions between neighboring segments. It is suggested that for the large m members these features represent a good compromise between the CDW instability of the metallic bronzes, related to their quasi-1D electronic structure, and the incipient antiferroelectric lattice distortion of the insulating oxide WO_3 , which corresponds to the limit $m \rightarrow \infty$ of this series. These structural features play a crucial role in setting the coupling between the differently oriented 1D portions of the Fermi surface required for the hidden nesting mechanism at the basis of the stabilization of a CDW ground state in the ReO_3 -type metallic W and Mo bronzes and oxides.

I. INTRODUCTION

A. Generalities

Beside the cuprates with high-temperature superconductivity, $(AO)_n(A'CuO_{3-x})_m$,¹ the manganites with colossal magnetoresistance, $Ln_{1-x}A_xMnO_3$,² and the spin gap vanadates AV_2O_5 ,³ the monophosphate tungsten bronzes with pentagonal tunnels, MPTBp, $(PO_2)_4(WO_3)_{2m}$,⁴ form a new family of oxides exhibiting low dimensional metallic properties together with charge-density-wave (CDW) instabilities.

Several members of the MPTBp family ($2 \leq m \leq 14$) have been isolated and characterized by single-crystal x-ray-diffraction, diffuse scattering, and conductivity measurements.⁵⁻⁷ Examination of the different crystal structures determined for the $m=2, 4, 5, 6, 7, 8$, and 12 members,⁸⁻¹⁴ leads to the same general building principle with only local variations, which induce slight distortions and symmetry changes. All these structures can be described by a regular stacking of perovskite WO_3 -type slabs, whose thickness increases with m . These slabs are connected through PO_4 tetrahedra so that large O_{18} cages with pentagonal windows are formed at the junction. These cages are either empty or can be partially occupied by Na^+ cations, as recently found in the $Na_x(PO_2)_4(WO_3)_{2m}$ series for $0 \leq x \leq 1$ and $m \geq 6$.¹⁵ Each tetrahedral (PO_2) group behaves as an electron reservoir which donates one electron to the WO_3 slabs. In $(PO_2)_4(WO_3)_{2m}$ this charge transfer to the WO_3 slabs leads to an average electron concentration of $2/m$ electron per W atom, and thus to a metallic behavior. However, when m increases, the decrease of carrier density, and the

concomitant reduction of screening of the Coulomb repulsions, will certainly enhance the electron-electron interactions. Finally, it is interesting to remark that the antiferroelectric (AFE) insulator WO_3 corresponds to the limit $m \rightarrow \infty$ of the MPTBp family.

B. CDW instabilities of the MPTBp's

In the structure of the MPTBp's each WO_3 -type slab can be decomposed into three arrays of parallel chains running along the $\mathbf{a} \pm \mathbf{b}$ and \mathbf{a} directions. Each chain is composed of segments of m corner-sharing octahedra. Band-structure calculations, using a tight-binding extended Hückel approximation, show that a quasiplanar Fermi surface (FS) can be associated to each chain array.¹⁶ As a result, the total FS can be approximately described by the superimposition of three FS sheets, each being perpendicular to a given chain direction. Each type of chain can undergo a $2\mathbf{k}_F$ CDW instability, \mathbf{k}_F being the Fermi wave vector related to its one-dimensional (1D) band structure. In agreement with this expectation, x-ray diffuse scattering experiments have revealed such 1D-CDW instabilities, especially for the low m (i.e., $m \leq 8$) members.⁵ Below a critical temperature T_c , these instabilities condense into a 3D ordered CDW ground state. For the $m \leq 6$ members, the critical wave vector of the CDW modulation observed below T_c can be accounted for by a hidden FS nesting mechanism¹⁷ which connects the crossing points of a couple of two differently oriented quasiplanar FS. In these members several successive CDW transitions have been observed, due to the different ways to couple the differently oriented quasi-1D FS.

For the $m \leq 8$ members, incommensurate CDW transitions with T_c ranging between 30 and 220 K have been observed. However, it should be noted that while the $m = 4, 5,$ and 6 members exhibit several successive incommensurate sinusoidal-like modulations with similar wave vectors,¹¹ the $m = 7$ and 8 members show complex CDW incommensurate modulations with many harmonics.^{5,18} Only short-range-order modulations were observed in the $m = 8$ member.¹⁸ For the $m \geq 9$ members, several structural phase transitions with T_c ranging from 330 to 730 K have been detected. Depending on m , their critical wave vector (denoted \mathbf{q}_d , $\mathbf{q}_{d'}$, and \mathbf{q}_0 below) has been found to be either in commensurate or incommensurate relationship with the reciprocal wave vectors of the MPTBp lattice.⁶

The assignment of the CDW instabilities to the WO₆ chains running along the \mathbf{a} and $\mathbf{a} \pm \mathbf{b}$ directions can easily be done for the low m members ($m \leq 8$) owing to the observation below room temperature (RT) of x-ray diffuse scattering pretransitional fluctuations under the form of diffuse sheets perpendicular to the \mathbf{a} or $\mathbf{a} \pm \mathbf{b}$ chain directions. On the contrary such assignment cannot be unambiguously performed for the high m members ($m \geq 9$) because the phase transitions occur above RT in a temperature range where there is in addition a strong anisotropic diffuse scattering due to thermally excited low-frequency phonon modes.

For the $m \geq 9$ members, in addition to the CDW instabilities of modulation wave vectors \mathbf{q}_d and/or $\mathbf{q}_{d'}$, a simple commensurate modulation of critical wave vector \mathbf{q}_0 , which component is $\frac{1}{2}\mathbf{a}^*$ in the (\mathbf{a}, \mathbf{b}) plane, was found.⁶ While $\mathbf{q}_d = \mathbf{q}_0$ for the $m = 9$ member, \mathbf{q}_d remains close to \mathbf{q}_0 for the $m = 10$ and 11 members. The $\mathbf{q}_{d'}$ instability, of smaller critical wave vector, becomes the dominant one for the $m = 12$ and 13 members. The $m = 14$ member apparently exhibits only the \mathbf{q}_0 modulation. The mechanisms at the origin of such complex phase diagrams are not clearly understood. A possible explanation, proposed in Ref. 6, is that, as the thickness of the WO₃ slabs increases with m , the layered MPTBp's may develop the AFE instability of the 3D perovskite WO₃, which critical wave vector, located at \mathbf{q}_0 in the MPTBp frame, could be, by its closeness, in competition with the \mathbf{q}_d CDW instability of the metallic layers.

C. $m = 10$ member

In order to understand more deeply the relationship between the various CDW instabilities undergone by the MPTBp's a detailed structural determination of their modulated phases is required. Such a structural determination is the object of the present paper. It concerns the $m = 10$ member (P₄W₂₀O₆₈), which also offers the opportunity to study the competition between the \mathbf{q}_d and \mathbf{q}_0 structural instabilities.

The $m = 10$ member is a poor metal. Preliminary measurements¹⁹ show that its electrical resistivity, which basically increases on cooling from 600 K (the highest temperature measured) until about 200 K, exhibits a weak bump at 460 K followed by a swallow minimum around 430 K. The $m = 10$ member, as well as the $m = 11$ member, behaves in an unusual manner, with respect to the other members, because its CDW critical wave vector \mathbf{q}_d varies in temperature.⁶ The high-temperature pretransitional structural fluctuations of the $m = 10$ member appear under the form of

broad diffuse segments centered at $\mathbf{q}_d \approx \mathbf{q}_0 = \frac{1}{2}\mathbf{a}^*$ and extending in the interslab \mathbf{c}^* direction. They can be detected until about 600 K. On cooling down the diffuse scattering sharpens and in the same time \mathbf{q}_d decreases. At about 400 K this wave vector locks in at the commensurate value $\mathbf{q}_d = \frac{3}{7}\mathbf{a}^*$, which is the value observed at RT, temperature at which the modulated structure has been refined in the present paper. The T_c of the CDW transition is estimated at about 450 K, temperature at which there is an anomaly in the thermal dependence of the resistivity.

II. EXPERIMENT

A. Synthesis and sample preparation

Platelike dark blue crystals of P₄W₂₀O₆₈ ($m = 10$) were prepared by the chemical vapor transport technique using the following procedure. A mixture of (NH₄)₂HPO₄ and WO₃ was first heated at 600 °C in air during 12 h to decompose the ammonium phosphate. An appropriate amount of metallic tungsten powder was then added before the mixture was heated in an evacuated silica ampoule at 1000 °C during 2 days. A portion of about 2 g of the resulting polycrystalline sample was then subsequently taken for the crystal growth, which was carried out in a quartz tube 20 cm long and 1.8 cm internal diameter. After sealed under vacuum, the tube was introduced in an horizontal furnace with a temperature gradient of about 10 °C/cm between the hot zone (1200 °C) and the cold zone (1000 °C). The tube was kept under these conditions during two weeks. Platelike crystals grew in the central part of the tube.

B. Preliminary x-ray photographic study

A lot of crystals obtained from the different preparations were tested by the inspection of x-ray patterns obtained from single-crystal rotating and Weissenberg methods. Weissenberg photographs showed that nearly all the samples were of poor quality with a stacking disorder revealed by the appearance of diffuse streaks sometimes more intense than the fundamental Bragg reflections. However, among the hundred of crystals tested, two crystals showed well defined Bragg spots with no diffuse lines. The best crystal was studied in detail and its diffracted intensity was registered later on an automatic diffractometer. The unit-cell parameters found are those expected for the $m = 10$ compound ($a = 5.3 \text{ \AA}$; $b = 6.5 \text{ \AA}$, $c = 35.8 \text{ \AA}$), attesting the obtention of P₄W₂₀O₆₈. As usual, the crystal was a (001) plate, with [110] as the long direction. The crystal was mounted with the \mathbf{b} axis as the rotation axis and Weissenberg patterns from $[h0l]$ to $[h3l]$ layers were taken. Satellites of first and second order were evidenced on each side of the festoons of the fundamental Bragg reflections. In agreement with previous x-ray diffuse scattering investigations,⁶ festoons of intense first-order satellite reflections, at the $\frac{3}{7}\mathbf{a}^*$ and $\frac{4}{7}\mathbf{a}^*$ [i.e., $(1 - \frac{3}{7})\mathbf{a}^*$] reduced wave vectors, as well as festoons of weaker second-order satellite reflections, at the $\pm \frac{1}{7}\mathbf{a}^*$ reduced wave vectors, were observed. No festoons of third-order satellite reflections, at the $\pm \frac{2}{7}\mathbf{a}^*$ reduced wave vectors, could be detected (they were, however, detected in the preliminary study reported in Ref. 5). This provides evidence for a structural

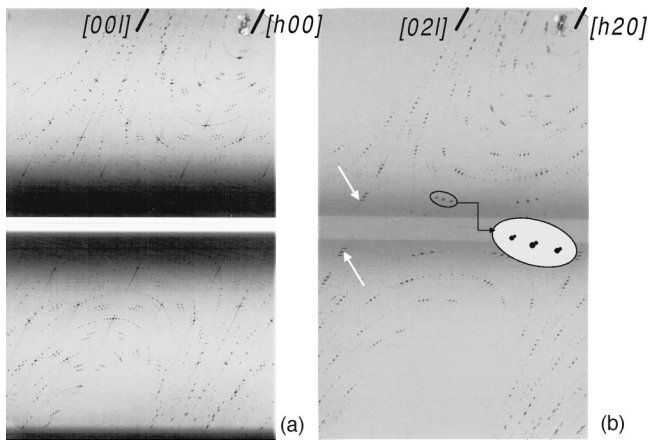


FIG. 1. Weissenberg patterns of the RT modulated structure of $P_4W_{20}O_{68}$. (a) $h0l$ layer: note the occurrence of satellite reflections by “waves.” (b) $h2l$ layer: note that the fundamental reflections are splitted while the satellite reflections seem to be unique. Note also the deformation of the $[02l]^*$ row for weak θ values, which is consistent with a monoclinic lattice symmetry (white arrows).

lattice modulation at the critical wave vector $\mathbf{q}_d = \alpha \mathbf{a}^*$ at RT, $\alpha = \frac{3}{7}$, within experimental errors.

The zero layer Weissenberg pattern [Fig. 1(a)] shows a single set of festoons of main Bragg reflections. However, in the upper layers, one observes a splitting of these festoons, which increases when k increases. This splitting is clearly visible for the $k=2$ layer Weissenberg pattern shown Fig. 1(b). Moreover, these patterns show that the rows parallel to \mathbf{a}^* appear always under the form of straight lines, whereas those parallel to \mathbf{c}^* are often deformed in the central part. These observations are consistent with the presence of a twin made of two monoclinic lattice variants; the monoclinic lattice can thus be viewed as due to a weak distortion of an orthorhombic lattice in the (\mathbf{a}, \mathbf{b}) plane, which leads to a γ angle different of 90° . The twofold axis is then the \mathbf{c} axis and/or the lattice mirror is the (001) plane. This setting was kept in the following because it corresponds to that already used for the MPTBp series of orthorhombic or pseudo-orthorhombic symmetry, where \mathbf{c} always corresponds to the largest unit cell parameter.

The symmetry element of the twin is either a (100) mirror or a $[010]$ twofold axis. In the reciprocal space, the \mathbf{c}^* and \mathbf{c}'^* reciprocal vectors of the two variants as well as \mathbf{a}^* and \mathbf{a}'^* are oriented in opposite direction, whereas \mathbf{b}^* and \mathbf{b}'^* are separated by an angle of 1.2° ($2 \times 0.6^\circ$) (Fig. 2). In the direct space, \mathbf{a} and \mathbf{a}' made the complementary angle, while the \mathbf{b} and \mathbf{b}' directions are the same and those of \mathbf{c} and \mathbf{c}' are opposite. Unfortunately, the existence of monoclinic twins, which is due to the ferroelastic character of the high-temperature phase transition,⁶ prevents us to find an untwinned crystal at RT. The structure was thus solved from the twinned crystal.

Surprisingly, the Weissenberg patterns taken from the upper layers do not reveal such a splitting for the festoons of first- and second-order satellite reflections. Possible explanations could be: (i) that the intensity of the satellite reflections due to the second component is too weak, or (ii) that the modulated structure is due to a particular arrangement of the twinned structural blocks. The first explanation is incompat-

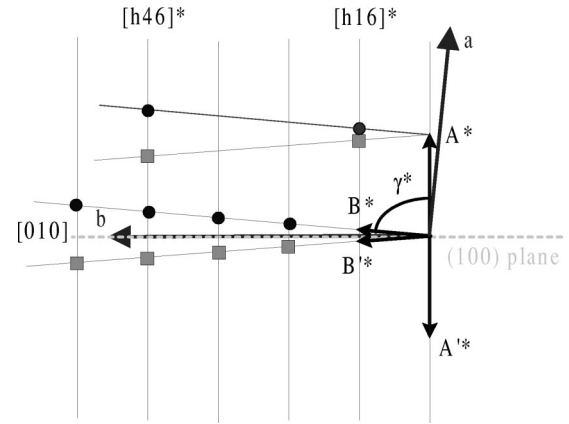


FIG. 2. Schematic representation in the reciprocal space of the splitting of the Bragg reflections due to the twinning.

ible with the observation of nearly all the fundamental reflections for the two variants, even the weakest ones. The second explanation could account for the observations if the satellite reflections were only issued from the block arrangement of a polysynthetic twin, each block itself contributing to the fundamental reflections. Calculations based on the approach developed by H. Böhm²⁰ show that this explanation induces satellite extinction conditions which are not observed. To elucidate this intriguing point, we have performed a diffractometer (Enraf Nonius CAD4) investigation of the crystal.

C. X-ray diffractometer investigation

To study accurately the twin effects, profiles of the reciprocal rows ranging from $[h06]^*$ to $[h56]^*$ both with $h > 0$ and $h < 0$ have been collected. This data collection supports quite well the previous twin hypothesis. However, as the γ angle remains close to 90° , the \mathbf{d}^* distance between the two reciprocal lattices is always small: $\mathbf{d}^*/\mathbf{a}^*$ being less than 0.02 for the $[h16]^*$ row and less than 0.07 for the $[h46]^*$ row.

As observed on the Weissenberg patterns (Fig. 1), the strongest fundamental reflections appear on “waves” on each festoon. Thus along a row such as $[h46]^*$, one observes fundamental reflections of strong intensity mostly for positive integer h values (Fig. 3), whereas those of negative

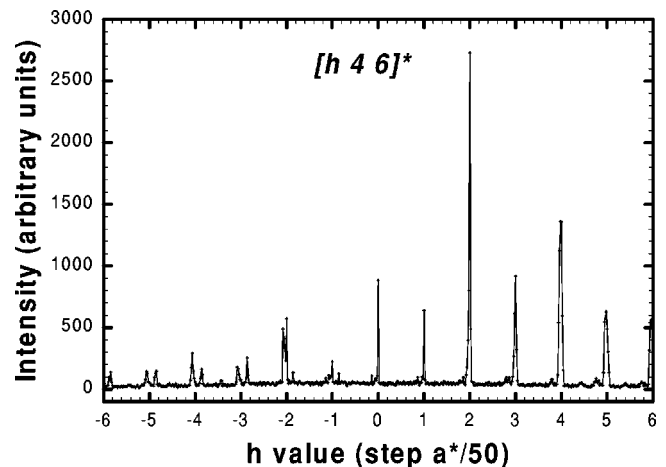


FIG. 3. Scan (by step of $\mathbf{a}^*/50$) of the $[h46]^*$ row. Note that main Bragg reflections belonging to a single twin are observed for $h > 0$.

h values are systematically weak. In this scan the (246) reflection appears to be unique, with an intensity of about 2700 on an arbitrary scale. It thus arises from a single twin component, say A . However, around the symmetrical $\bar{2}46$ reciprocal position two small peaks appear; one peak is just located at the reciprocal coordinate ($\bar{2}46$), with an intensity of about 600, and the other one, of an intensity of about 500, is located on its left side. This second peak is due to the twinning: it corresponds to the (246) reflection of the second component, say B . If we consider only the heights of the peaks one can estimate a twin ratio of about 18% (500/2700). At the ($\bar{2}46$) reflection of the A component corresponds also the ($\bar{2}46$) peak of the B component with an intensity of the order of $600 \times 0.18 = 108$ lost in the foot of the intense (246) reflection of the A component and thus not visible on the scan of Fig. 3. Along this row, there is no intensity detectable at the $\bar{3}46$, $\bar{4}46$, and $\bar{5}46$ reciprocal positions. The structure factor (F) of the corresponding Bragg reflections should be very weak. However, there are two peaks which appear in their neighborhood. They are due to the twin component B for the left ones and to the satellites of second order for the right ones.

The analysis of such scans explain well the quasisystematic splitting observed in the x-ray patterns for the fundamental reflections: if the structure factors of both the ($h46$) and ($\bar{h}46$) reflections are noticeable, the twin law induces a systematic doubling of the peaks. On the contrary, if one of the reflection, say ($\bar{h}46$), is very weak, and if the other reflection, ($h46$), is significant, only an unique peak will be observed. Because of the twin effect, its equivalent reflection, which corresponds to the second component of the twin, will also be observed alone, close to a point of integer coordinates. When this phenomenon takes place for several fundamental reflections it should be used profitably to refine the unit-cell parameters, as described in details elsewhere.¹¹ Thus by centering a great number of such unique peaks the crystal orientation of one of the twin components can be reached (Table I).

The same features are observed for the satellite reflections. For examples in the scan of the $[h36]^*$ row (Fig. 4), the first-order satellite reflections with $h < 0$ are well defined while those with $h > 0$ are broadened. For $h < 0$ the well splitted satellites, of reduced wave vectors $\pm \frac{3}{7}\mathbf{a}^*$, belong to a single twin while the ones for $h > 0$ are broadened because the twinning duplicates them.

Several conclusions can be drawn at this stage: (i) P₄W₂₀O₆₈ has a monoclinic pseudoorthorhombic lattice with the largest parameter \mathbf{c} being the twofold axis, (ii) the existence of a systematic twin phenomenon is confirmed and all the positions of the observed reflections are well identified, (iii) from the important asymmetry observed between the diffracted intensities, the actual symmetry should be quite different from the expected orthorhombic one (the intensity difference is certainly amplified by the presence of heavy atoms such as the W), and (iv) there is a lattice modulation giving rise to satellite reflections with a strong intensity, as shown Fig. 4. Despite all these difficulties, the quality of the present crystal gave the opportunity to investigate the structural origin of the CDW modulations observed, but still not

yet elucidated, in the (PO₂)₄(WO₃)_{2 m} series. It was thus decided to collect the intensity of fundamental and satellite reflections and to solve the modulated structure using the four-dimensional (4D) superspace formalism.

D. Registration of the diffracted intensity

The conditions used for the data collection are in Table I. The intensity of the fundamental reflections has been collected first, then the intensity of the satellites of first order and finally that of the satellites of second order. Satellites were recorded using the program SAT.²¹ The registration has been performed during more than one month. For each fundamental reflection, the type of scan and its angular range have been chosen in order to include systematically the two components of the twin without overlapping the closest satellites. The result of this procedure has been scrupulously verified on each intensity profile before the data analysis. More than 104 000 reflections measured in two equivalent monoclinic areas have been corrected as usual (Lorentz and polarization, standards, absorption effects). The reflections having a too weak intensity [$I \leq 3\sigma(I)$] and those with doubtful profiles have been rejected. The absorption corrections, using crystal morphology²² have been performed after measurement of the crystal size with a microscope, *in situ* location of the faces indices, and verification of their indexation with an optical two-circle goniometer. The twin effect has also been corrected. All these corrections have been done using the JANA98 program.²³

III. RESOLUTION OF THE STRUCTURE

A. Crystal symmetry

The 4D approach appears to be more suitable than the classical formalism, based on the supercell ($7\mathbf{a}, \mathbf{b}, \mathbf{c}$), to solve the modulated structure for several reasons: (i) it leads to a better description of the crystal symmetry, thus defined from a 4D group rather than from a classical 3D one,²⁴ (ii) it introduces modulation functions allowing to describe the distortion of the basic structure by atomic displacement waves running along [100], and (iii) it mainly reduces the number of parameters which have to be refined knowing that all the orders of the satellite reflections are not observed. In this respect, the observation of only first- and second-order satellite reflections justifies this procedure.

Within this framework, the complete diffraction pattern can then be indexed with four integer indices $hklm$ with respect to the set of basis vectors \mathbf{a}^* , \mathbf{b}^* , \mathbf{c}^* , and \mathbf{q}_d , where $\mathbf{q}_d = \alpha\mathbf{a}^*$ ($\alpha = \frac{3}{7}$) is the modulation wave vector and m the satellite order. The modulation is of the planar monoclinic type,²⁵ i.e., \mathbf{q}_d is parallel to the mirror (001). The only extinction rule, $l = 2n + 1$, observed for the (00 l) reflections leads to the super space group $P2_1(\alpha 00)0$.

In a crystal characterized by a one-dimensional incommensurate modulation, all the sections t of the 4D space are equivalent. They lead to the same modulated structure in the physical 3D space modulo an arbitrary phase shift. In contrast, if the modulation is commensurate, only some sections describe the actual symmetry of the crystal. In the present case, only one type of section of monoclinic symmetry has been considered: it is defined by $t = v/14$,²⁶ where v is an

TABLE I. Crystal data and details of the structural refinement.

Crystal data		
Empirical formula	$P_4W_{20}O_{68}$	
Formula weight	4888.8	
Crystal system	monoclinic	
Super space group	$P2_1 (\alpha 00) 0$	
a, b, c [Å]	5.305(2)	6.551(2) 35.823(8)
α, β, γ [°]	90 90 90.62(3)	
V [Å ³]	1244.8(6)	
Z	1	
D (calc) [g/cm ³]	6.519	
F (000)	2084	
μ (Mo $K\alpha$) [cm ⁻¹]	462.6	
Data collection		
Temperature [K]	293	
Radiation [Å]	Mo $K\alpha$ $\lambda = 0.71073$	
θ range [°]	2 45.0	
Scan (type and range) [°]	3, 1+0.35 tan(θ) for fundamentals 3, 0.6+0.35 tan(θ) for satellites	
Dataset	- 10: h :10; - 13: k :13; 0: l :70; - 2: m :2	
Recorded reflections (two independent monoclinic spaces):		
Fundamental 1st order, 2nd order	20611, 41337, 41250	
Recorded unique reflections:		
Fundamental, 1st order, 2nd order	10337, 20674, 20630	
Observed data [$I \geq 3.0\sigma(I)$]		
Fundamental 1st order, 2nd order	6146, 4831, 1906	
Used unique reflections:		
Fundamental, 1st order, 2nd order	3212, 3111, 1403	
Refinement		
N par	596	
$R_{\text{tot}}, R_0, R_1, R_2$	8.67, 6.70, 10.01, 14.48	
Secondary extinction type I	0.179(5)	
Max and min electron residual	$+1.4e^-$, $-1.2e^-$ (at ≈ 0.6 Å of W1a)	
Weighting scheme	unit	
Twin ratio	0.15(1)	

integer. Thus, the modulated structure of $P_4W_{20}O_{68}$ was refined in the particular section $t=0$. The 3D space group (SG) related to the supercell structure turns then to be $P2_1$, the SG of the average structure.

B. Average structure

The only extinction condition observed in the set of fundamental reflections are for $(00l)$ with $l=2n+1$, consistent with the presence of a twofold axis 2_1 along $[001]$. Other extinction conditions, such as those due to a n glide plane normal to \mathbf{c} , are only approximate. The strategy used to solve the structure of the $m=10$ member was to start with the idealized $P2_12_12_1$ space group (such an orthorhombic lattice description, which is that of the even m members of the series, governs all the tilting of the WO_6 octahedra), then to deduce the amplitude of the atomic displacements and to continue the refinement in the $P2_1$ group with \mathbf{c} as the twofold axis. The average structural model agrees well with that

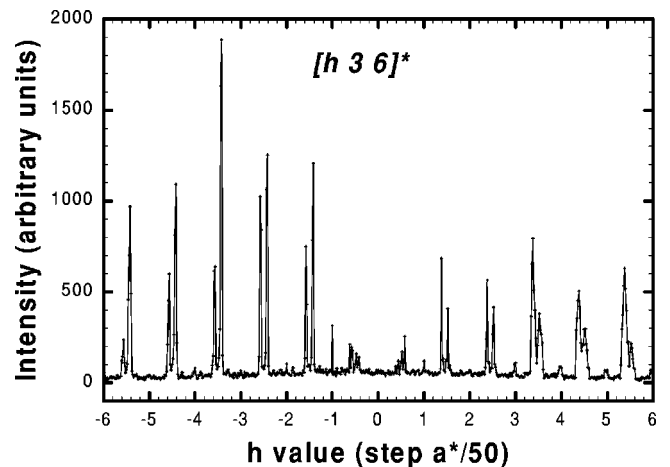


FIG. 4. Scan (by step of $a^*/50$) of the $[h36]^*$ row. Note that well splitted first-order satellite reflections belonging to a single twin are observed for $h < 0$. The four satellites due to twinning are only observed for $h > 0$.

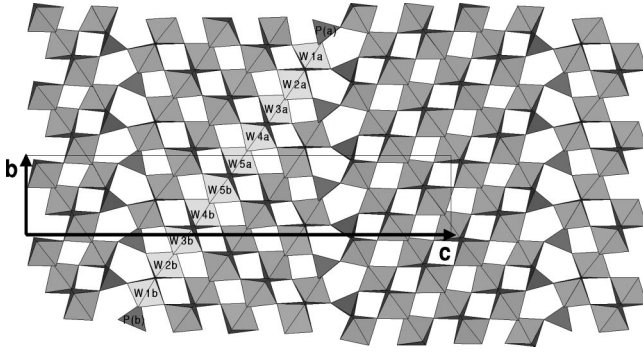


FIG. 5. Projection along (100) of the average structure of P₄W₂₀O₆₈ ($R = 0.067$ for 3212 reflections and 237 parameters). This figure shows the tilting of the octahedra, which remains compatible with the orthorhombic space group $P2_12_12_1$. A segment of ten WO₆ octahedra delimited by two PO₄ tetrahedra, together with the labeling of its W atoms, is highlighted.

describing all the members of the (PO₂)₄(WO₃)_{2m} series whose structure is known ($m = 4, 5, 6, 7, 8, 12$). The crystal structure results from the regular stacking of WO₃-type slabs, all of the same thickness, interconnected with slices of PO₄ tetrahedra. It is also possible to describe the slabs as a set of parallel chains of WO₆ octahedra sharing corners in one of the three main Cartesian directions of the perovskite structure: for example five octahedra in the approximate direction $[0 \bar{4} 1]$, nearly all tilted in the same sense, or ten octahedra in the directions close to $[12 \ 8 \ 1]$ or $[\bar{1}2 \ 8 \ 1]$, as shown in Fig. 5. This last description, which involves the thickness parameter m , remains valid whatever m .

C. Modulated structure

The components of the displacement vector \mathbf{U}^μ of the μ th atom were written as Fourier series limited to the first and second harmonics since the satellite reflections with $|m| > 2$ were not observed, leading to the relation

$$U_i^\mu(\bar{x}_4^\mu) = \sum_{n=1}^2 A_{i,n}^\mu \cos(2\pi n \bar{x}_4^\mu) + B_{i,n}^\mu \sin(2\pi n \bar{x}_4^\mu) \\ (i = 1, 2, 3).$$

In this expression $\bar{x}_4^\mu = \mathbf{q}_d \cdot (\mathbf{r}_0^\mu + \mathbf{p}) = \mathbf{q}_d \cdot \mathbf{r}_0^\mu + s$ is an internal parameter, \mathbf{r}_0^μ defines the average position of the μ th atom in the origin unit cell ($\mathbf{a}, \mathbf{b}, \mathbf{c}$) and \mathbf{p} is a lattice vector; only the $s = 0, \frac{1}{7}, \frac{2}{7}, \frac{3}{7}, \frac{4}{7}, \frac{5}{7},$ and $\frac{6}{7}$ values are physical points.

To determine a model for the displacive modulation, 4D Patterson maps were calculated from the whole set of reflections. In the favorable case, where no fortuitous peak superposition occurs, it is possible to derive both the amplitude and the phase (with an uncertainty of π) of the displacement function of the μ th atom.²⁷ It is thus sufficient to perform a map about one Harker peak of this atom. Because of the pseudo-orthorhombic symmetry which leads for the W atoms to superimposed Harker peaks, this method did not allow to obtain reliable results. A trial and error method was then used by estimating the displacement amplitudes of the W from the anisotropic thermal parameters derived from the study of the average structure. In the initial stage of the re-

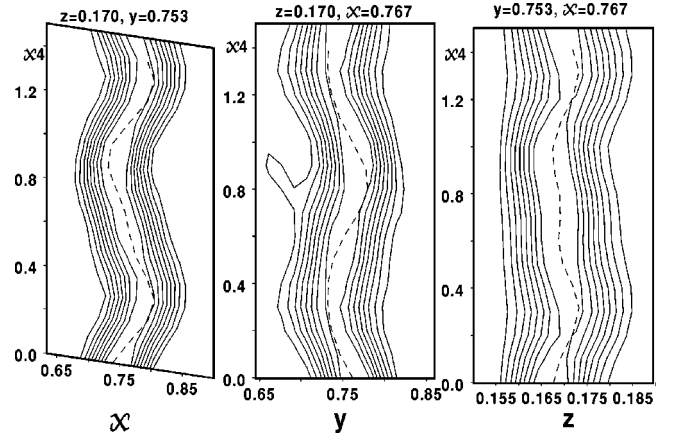


FIG. 6. Four-dimensional Fourier map (F_{obs}) along $x, y,$ and z around the W1a atom. The dashed lines represent the model used in the refinement. Contour's interval are $55e^{-7}/\text{\AA}^3$.

finement, only the first harmonics were introduced and arbitrary phases were given to the displacement functions. Fortunately, as the amplitudes of the displacement are small, the convergence was ensured in spite of the wrong initial phases. The second harmonics were then introduced to improve the previous model.

Refinements showed that W atom positions undergo a significant modulation, as also proved from Fourier maps around the W1a (see Fig. 6). On the contrary, oxygen and phosphorus displacements are negligible and consequently the polyhedral building is not disturbed nor distorted through the modulation effects. So, the tilting of all the octahedra remains similar to that given by the $P2_12_12_1$ space group found for the other even m members (Fig. 5).

As previously found by Frost-Jensen *et al.*,²⁸ the introduction of a modulation of the thermal parameters of some atoms in the refinement of a modulated structure can lead to a significant improvement of the reliability R factor. Such a modulation was assumed for the W atom. It leads to a R decrease from 18.4 to 14.5% for second-order satellites, and from 12.5 to 10.0% for the first-order satellites. The main reflections are less affected by the modulation of the thermal parameters (R decreasing from 8.0 to 6.7%). The physical explanation of such an effect is that, because of the displacive modulation, the surrounding of the W atoms changes with the internal parameter s in a noticeable way throughout the crystal. Thus, as the interatomic potential varies with s , the atomic thermal motion becomes also a function of s .

Though the R factors are rather high, it is clear that the basic features of the modulated structure appears to be reliable. However, it should be outlined that the anisotropic thermal parameters of W1a, W2a, and W4b atoms cannot be defined within a classical ellipsoid model. This may be due to insufficiencies in the absorption corrections or in the twin corrections. Further, it must be kept in mind that the structure is intrinsically complex to solve: (i) it is a modulated and twinned structure with a rather long \mathbf{c} parameter rendering the intensity measurements tricky, (ii) the absorption coefficient is high ($\mu_{\text{Mo}} = 463 \text{ cm}^{-1}$) and the crystal shape is complex and difficult to model, (iii) the structure is pseudo-symmetric which limits the convergence of the refinement because of the introduction of likely correlated parameters,

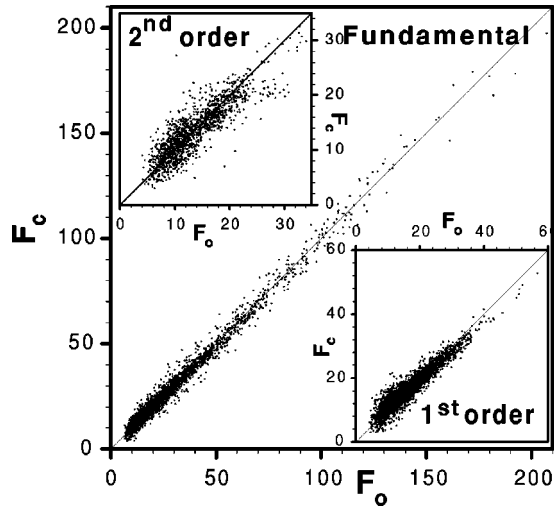


FIG. 7. Observed (F_o) vs calculated (F_c) structure factors for the different classes of reflections considered in the text. The linearity assesses the quality of the data and of the refinement.

(iv) there are about 600 parameters to refine simultaneously, and, finally, (v) the presence of stacking faults involving WO_3 -type slabs of different thickness and/or of slabs undergoing a $\mathbf{q}_0 = \frac{1}{2}\mathbf{a}^*$ modulation (as revealed by the presence of residual diffuse streaks on the x-ray patterns of samples studied in Ref. 6) cannot be completely ruled out.

TABLE II. Fractional atomic coordinates and RT Fourier amplitudes of the modulation function of the tungsten atoms of $\text{P}_4\text{W}_{20}\text{O}_{68}$ (labeling given Fig. 5).

Atom	wave	x	y	z	Atom	wave	x	y	z
W1a	r_0^μ	0.5177(3)	0.7523(4)	0.1697(1)	W1b	r_0^μ	0.0135(4)	0.2530(4)	0.2876(1)
	$B_{i,1}^\mu$	0.0245(6)	-0.0214(7)	0.0020(1)		$B_{i,1}^\mu$	0.0031(5)	0.0006(5)	-0.0009(1)
	$A_{i,1}^\mu$	-0.0206(6)	0.0114(5)	-0.0010(1)		$A_{i,1}^\mu$	0.0018(5)	-0.0003(6)	-0.0005(1)
	$B_{i,2}^\mu$	0.0008(8)	-0.0006(8)	-0.0011(2)		$B_{i,2}^\mu$	0.0084(8)	0.0028(8)	-0.0011(2)
	$A_{i,2}^\mu$	-0.0112(8)	-0.0005(8)	-0.0009(2)		$A_{i,2}^\mu$	0.0047(8)	0.0035(9)	0.0006(1)
W2a	r_0^μ	0.0119(4)	0.0852(4)	0.1278(1)	W2b	r_0^μ	0.5208(4)	0.5990(5)	0.3300(1)
	$B_{i,1}^\mu$	0.0250(7)	-0.0149(7)	0.0020(1)		$B_{i,1}^\mu$	-0.0121(7)	0.0124(8)	0.0008(1)
	$A_{i,1}^\mu$	0.0167(7)	-0.0149(6)	0.0007(1)		$A_{i,1}^\mu$	0.0048(6)	-0.0050(6)	-0.002(1)
	$B_{i,2}^\mu$	-0.0029(8)	0.0010(6)	-0.0004(1)		$B_{i,2}^\mu$	-0.002(1)	0.0040(9)	0.0010(2)
	$A_{i,2}^\mu$	0.0108(9)	-0.0152(7)	0.0022(1)		$A_{i,2}^\mu$	0.003(1)	-0.008(1)	-0.0008(2)
W3a	r_0^μ	0.5059(4)	0.4195(6)	0.0847(1)	W3b	r_0^μ	0.0168(5)	0.9222(4)	0.3744(1)
	$B_{i,1}^\mu$	-0.0101(7)	0.0004(9)	-0.0016(1)		$B_{i,1}^\mu$	-0.0032(7)	0.0031(6)	0.0000(1)
	$A_{i,1}^\mu$	0.0229(7)	-0.0118(7)	0.0022(1)		$A_{i,1}^\mu$	-0.0187(8)	0.0070(8)	0.0007(2)
	$B_{i,2}^\mu$	0.006(1)	0.0120(9)	-0.0011(2)		$B_{i,2}^\mu$	0.005(1)	-0.001(1)	0.0001(2)
	$A_{i,2}^\mu$	-0.007(1)	0.002(1)	-0.0019(2)		$A_{i,2}^\mu$	-0.012(1)	0.006(1)	0.0006(2)
W4a	r_0^μ	0.0059(4)	0.7494(4)	0.0421(1)	W4b	r_0^μ	0.5088(4)	0.2604(4)	0.4153(1)
	$B_{i,1}^\mu$	-0.0250(6)	0.0182(6)	-0.0017(1)		$B_{i,1}^\mu$	-0.00116(7)	0.0121(7)	0.0003(1)
	$A_{i,1}^\mu$	-0.0169(7)	0.0164(8)	-0.0008(2)		$A_{i,1}^\mu$	-0.0239(6)	0.0176(5)	0.0031(1)
	$B_{i,2}^\mu$	-0.0177(9)	0.0056(8)	-0.0001(2)		$B_{i,2}^\mu$	0.0104(8)	-0.0140(8)	0.0007(2)
	$A_{i,2}^\mu$	0.0049(7)	-0.0036(7)	0.0013(1)		$A_{i,2}^\mu$	0.0252(8)	-0.0130(7)	-0.0021(1)
W5a	r_0^μ	0.4895(4)	0.0846(5)	0.0(0)	W5b	r_0^μ	0.0165(4)	0.5821(4)	0.4582(1)
	$B_{i,1}^\mu$	0.0066(8)	-0.003(1)	0.0014(1)		$B_{i,1}^\mu$	0.0201(7)	-0.0178(6)	-0.0022(1)
	$A_{i,1}^\mu$	-0.0203(7)	0.0132(7)	-0.0022(2)		$A_{i,1}^\mu$	-0.0054(8)	0.0009(7)	0.0003(2)
	$B_{i,2}^\mu$	-0.001(1)	-0.001(1)	-0.0013(2)		$B_{i,2}^\mu$	-0.007(1)	0.0181(7)	0.0009(2)
	$A_{i,2}^\mu$	-0.004(1)	0.000(1)	-0.0004(2)		$A_{i,2}^\mu$	-0.006(1)	0.0064(8)	0.0013(2)

In order to check the validity of the model, statistical tests, such as those recommended by Watkin,²⁹ were performed. Let us call F_o the observed structure factor and F_c the calculated one. The plot F_c vs F_o , shown in Fig. 7, gives the dispersion of the results for the fundamental as well as for the first- and second-order satellite reflections. One can see that there is, *a priori*, no systematic errors in the final results (as for instance a systematically overestimated value of F_c with respect to F_o). Similarly, the difference ($F_o - F_c$) vs $\sin \theta/\lambda$ showed no peculiarity, contrary to a previous study performed on a twinned crystal of the same family.¹¹ Moreover, the plots ($F_o - F_c$) vs h , k , and l revealed no anomaly for a special class of reflections (as for instance a better agreement for the low values of k). One can thus conclude, after this series of statistical tests, that there are no noticeable systematic errors in the last stage of the refinement of the modulated structure of $\text{P}_4\text{W}_{20}\text{O}_{68}$. Final atomic parameters for the tungsten atoms are listed Table II. Parameters corresponding to the anisotropic thermal parameters and to their modulation are available from the corresponding author. Final atomic and thermal parameters concerning the O and P atoms (i.e., the atoms which are not affected by the modulation) are given Table III. The interatomic distances in the average structure as well as the minimum and maximum distances in the modulated structure are given Table IV. A complete list of the O-O distances and the

TABLE III. Fractional atomic coordinates and isotropic displacement parameters (\AA^2) for the P and O atoms which are not affected by the modulation.

Atom	x	y	z	B (\AA^2)	Atom	x	y	z	B (\AA^2)
P(a)	-0.011(2)	0.449(2)	0.1988(5)	1.8(2)	O9a	0.779(5)	0.582(4)	0.0727(8)	1.1(3)
P(b)	-0.472(1)	0.942(1)	0.2592(3)	0.12(9)	O9b	0.738(4)	0.047(3)	0.3912(7)	0.5(3)
O1a	0.030(6)	0.264(5)	0.175(1)	1.3(5)	O10a	0.280(5)	0.624(4)	0.0633(8)	1.2(3)
O1b	0.499(5)	0.744(4)	0.2834(9)	0.7(3)	O10b	0.229(5)	0.095(5)	0.3994(9)	1.5(4)
O2a	0.016(5)	0.902(4)	0.0910(7)	0.7(3)	O11a	0.700(5)	0.897(5)	0.0269(9)	1.5(4)
O2b	0.519(5)	0.432(4)	0.3737(7)	0.6(3)	O11b	-0.191(5)	0.385(4)	0.4332(8)	1.1(3)
O3a	-0.211(0)	0.880(0)	0.1580(0)	0.8(3)	O12a	0.495(7)	0.241(5)	0.0479(9)	1.8(5)
O3b	-0.237(0)	0.420(0)	0.3050(0)	1.7(5)	O12b	0.015(4)	0.765(4)	0.4170(7)	0.7(3)
O4a	-0.288(4)	0.228(4)	0.1151(7)	0.8(3)	O13a	-0.225(4)	0.238(4)	-0.0143(6)	0.4(2)
O4b	0.803(4)	0.728(4)	0.3478(7)	0.8(3)	O13b	0.716(5)	0.710(4)	0.4776(9)	1.1(4)
O5a	0.220(4)	0.288(3)	0.1095(6)	0.4(2)	O14a	0.496(9)	0.590(7)	0.127(1)	1.0(0)
O5b	0.313(4)	0.766(4)	0.3544(7)	0.9(3)	O14b	0.015(5)	0.089(4)	0.3270(9)	0.7(3)
O6a	0.275(5)	0.911(5)	0.1566(9)	1.2(4)	O15a	0.215(4)	0.585(4)	0.1887(8)	0.7(3)
O6b	0.227(5)	0.438(5)	0.3069(9)	1.4(4)	O15b	0.320(5)	0.091(4)	0.2710(9)	1.3(4)
O7a	0.022(8)	0.588(7)	0.006(1)	1.0(0)	O16a	0.02(1)	0.360(8)	0.240(2)	1.0(0)
O7b	0.495(5)	0.091(4)	0.4592(8)	0.5(3)	O16b	0.510(5)	0.895(5)	0.2181(8)	0.8(3)
O8a	0.196(5)	0.946(4)	0.0201(8)	1.1(3)	O17a	0.732(4)	0.549(4)	0.1975(8)	0.9(3)
O8b	0.314(4)	0.432(4)	0.4403(8)	0.9(3)	O17b	-0.217(0)	0.050(0)	0.265(0)	1.9(5)

whole list of the W-O distances according to the internal parameter are available from the corresponding author. If the average W-O distances are considered, it should be noted that for the WO_6 octahedra located in the middle part of the slabs the six W-O distances are gathered about their mean value 1.92 \AA , as usual for all the other members of the MPTBp series ($m=4$ excepted) while for WO_6 octahedra on the sides of the slab, i.e., those close to the PO_4 tetrahedra, the six W-O distances are more spread, illustrating the fact that the W atoms are displaced with respect to the center of the oxygen octahedra.

IV. DISCUSSION

A. RT displacive modulation

The most important result of the refinement of the modulated structure of $P_4W_{20}O_{68}$ is that the displacive modulation involves mainly the W atoms inside the different WO_6 octahedra of the WO_3 -type slab. The best way to visualize these W displacements is to decompose the slab into segments of ten WO_6 octahedra sharing corners in the $[12\ 8\ 1]$ direction, as highlighted in Fig. 5. A given segment is bounded at each end by a PO_4 tetrahedron [P(a) or P(b)]. The W displacements, with respect to their position in the average structure, have been calculated for all the independent W atoms. They are represented Fig. 8 by arrows in a section of the WO_3 slab by a plane including the \mathbf{a} (vertical axis) and the $[12\ 8\ 1]$ directions. This figure, where the W displacements are, for clarity, magnified ten times, shows that the W atoms are mostly displaced in the direction of the segments of ten WO_6 octahedra, the maximum W displacement being of 0.19 \AA . In order to verify this assertion, i.e., to be certain that the displacement normal to the section plane is small, the segment highlighted on Fig. 8, for which the W displacements are the greatest, has been selected. The projection of the W displacements into the three (\mathbf{a} , \mathbf{b}), (\mathbf{b} , \mathbf{c}), and (\mathbf{c} , \mathbf{a}) basic planes

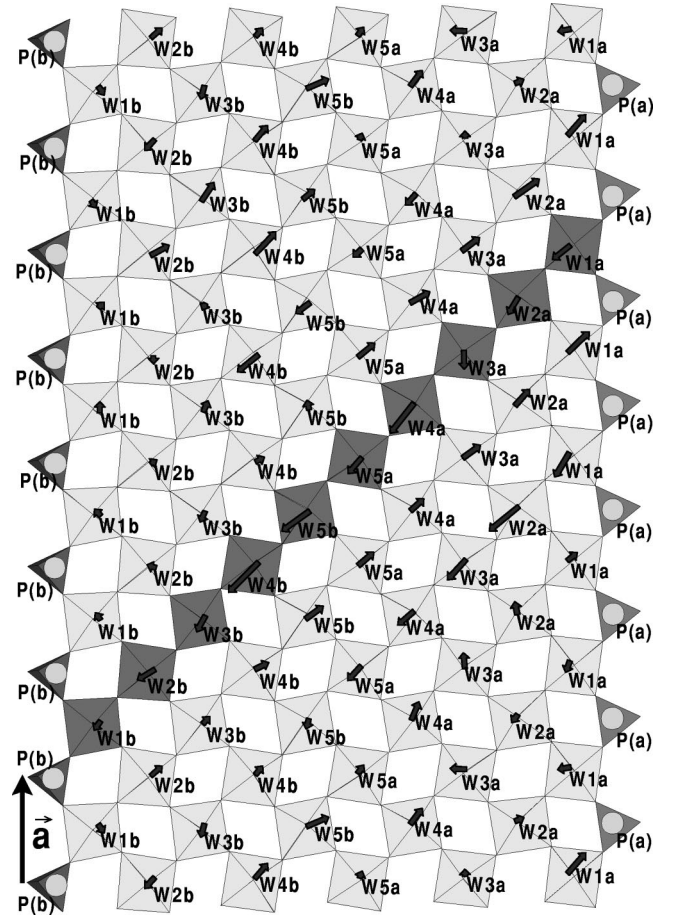


FIG. 8. Section of one WO_3 layer of the $7\mathbf{a} \times \mathbf{b} \times \mathbf{c}$ supercell of $P_4W_{20}O_{68}$ by a plane including the superstructure \mathbf{a} direction and the $[12\ 8\ 1]$ direction of the segment of ten WO_6 -octahedra outlined Fig. 5. The arrows represent, magnified by 10, the W displacements with respect to their position in the average P_2 structure.

TABLE IV. W-O and P-O interatomic distances (\AA) in the average structure and minimum/maximum W-O interatomic distances (\AA) in the modulated structure. A complete list has been deposited.

	Average	Min	Max	Average	Min	Max	Average	Min	Max	Average	Min	Max			
W1a-O3a	1.71 (1)	1.66	1.81	W1b-O3b	1.84 (3)	1.80	1.90	W2a-O1a	2.07 (4)	2.03	2.11	W2b-O1b	1.92 (3)	1.88	1.95
W1a-O6a	1.73 (3)	1.49	1.98	W1b-O6b	1.79 (3)	1.74	1.83	W2a-O2a	1.78 (3)	1.74	1.84	W2b-O2b	1.91 (3)	1.89	1.95
W1a-O14a	1.88 (5)	1.83	1.95	W1b-O14b	1.77 (3)	1.72	1.84	W2a-O3a	2.09 (1)	2.00	2.21	W2b-O3b	1.96 (3)	1.82	2.12
W1a-O15a	2.05 (3)	1.99	2.10	W1b-O15b	2.04 (3)	1.98	2.08	W2a-O4a	1.91 (2)	1.60	2.16	W2b-O4b	1.83 (3)	1.80	1.85
W1a-O16b	1.97 (3)	1.92	2.01	W1b-O16a	1.85 (6)	1.77	1.90	W2a-O5a	1.84 (2)	1.79	1.95	W2b-O5b	1.79 (3)	1.63	1.93
W1a-O17a	2.02 (3)	1.76	2.24	W1b-O17b	1.97 (2)	1.93	2.02	W2a-O6a	2.09 (3)	1.82	2.41	W2b-O6b	2.05 (3)	2.02	2.09
W3a-O4a	2.00 (3)	1.82	2.22	W3b-O4b	1.94 (3)	1.92	1.97	W4a-O2a	2.02 (3)	1.97	2.06	W4b-O2b	1.87 (3)	1.75	1.97
W3a-O5a	1.95 (2)	1.85	2.03	W3b-O5b	2.02 (3)	1.89	2.20	W4a-O7a	1.67 (5)	1.62	1.78	W4b-O7b	1.93 (3)	1.86	2.04
W3a-O9a	1.84 (3)	1.77	1.96	W3b-O9b	1.80 (2)	1.61	1.92	W4a-O8a	1.82 (3)	1.77	1.91	W4b-O8b	1.78 (3)	1.52	2.16
W3a-O10a	1.96 (3)	1.76	2.13	W3b-O10b	1.82 (3)	1.80	1.86	W4a-O9a	1.95 (3)	1.89	2.01	W4b-O9b	2.05 (2)	1.68	2.31
W3a-O12a	1.76 (3)	1.72	1.84	W3b-O12b	1.84 (3)	1.83	1.86	W4a-O10a	1.84 (3)	1.69	2.17	W4b-O10b	1.91 (3)	1.89	1.98
W3a-O14a	1.87 (5)	1.80	1.94	W3b-O14b	2.02 (3)	2.01	2.04	W4a-O11a	1.97 (3)	1.64	2.13	W4b-O11b	1.89 (3)	1.86	1.97
W5a-O7b	1.86 (3)	1.81	1.94	W5b-O7a	2.06 (5)	2.01	2.10								
W5a-O8a	1.92 (3)	1.90	1.95	W5b-O8b	1.98 (3)	1.70	2.15	P(a)-O1a	1.49 (4)			P(b)-O1b	1.57 (3)		
W5a-O11a	1.93 (3)	1.76	2.09	W5b-O11b	1.91 (3)	1.82	2.03	P(a)-O15a	1.53 (3)			P(b)-O15b	1.54 (3)		
W5a-O12a	2.00 (3)	1.92	2.06	W5b-O12b	1.90 (3)	1.87	1.96	P(a)-O16a	1.59 (7)			P(b)-O16b	1.51 (3)		
W5a-O13a	1.88 (2)	1.86	1.92	W5b-O13a	1.88 (2)	1.79	2.01	P(a)-O17a	1.52 (3)			P(b)-O17b	1.54 (1)		
W5a-O13b	1.92 (3)	1.76	2.08	W5b-O13b	1.94 (3)	1.78	2.21								

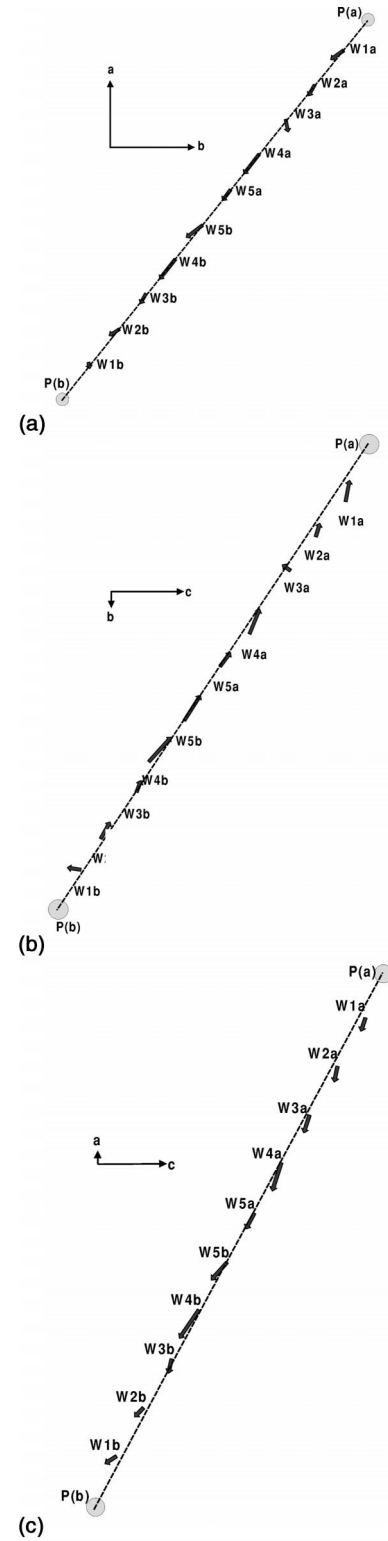


FIG. 9. Projection in the (a, b) plane in (a), (b, c) plane in (b), and (a, c) plane in (c) of the W displacements of the segment highlighted Fig. 8. This figure shows clearly that the W atoms are mostly displaced in the segment direction.

has been drawn in Figs. 9(a), 9(b), and 9(c), respectively. These figures confirm that the main direction of displacement of the W atom is along the segment direction, which confers to it a ferroelectric polarization. However if all the W atoms of this segment are displaced in the same direction, the

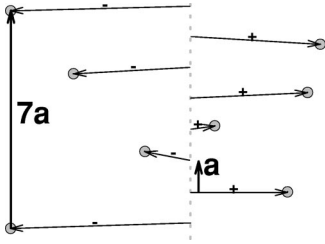


FIG. 10. Variation along the superstructure direction \mathbf{a} of the sum of the RT W displacements (i.e., the polarization) of each segment of ten octahedra represented Fig. 8.

amplitude of the displacement varies with the W atom. Finally, it is worth noticing that if one considers the segment of ten WO_6 octahedra oriented in the $[-12\ 8\ 1]$ direction of the slab, which is approximately perpendicular to the one along the $[12\ 8\ 1]$ direction, the W displacements are roughly perpendicular to the segment direction.

Figure 8 shows that the W displacements in the segments located on each side of the highlighted one are mainly oriented in the opposite direction. Such an alternate change of the main direction of W displacements from one segment to the next one cannot be repeated all over the WO_3 -type slab because the superstructure contains an odd number of \mathbf{a} periodicities. Thus with respect to the alternate order, the tungsten displacements must be either canceled or reversed in some segments in order to ensure the $7\mathbf{a}$ periodicity. In order to quantify this effect we have calculated the sum of the W displacements (i.e., the polarization) of each segment. Figure 10 shows how this vectorial quantity behaves for the seven segments of the unit cell along \mathbf{a} . If (+) and (−) denote the sense of the polarization of each segment, the sequence $\cdots(-)(+)(-)(+)(+)(-)(+)\cdots$ is observed in this direction. The superstructure thus includes a defect of alternation (i.e., of AFE order) every seven periodicities, which could give rise to a net polarization. More precisely, the results reported Fig. 10 show also that there is no real compensation between the polarization of the (+) and (−) sublattices and thus that each slab must exhibit a net polarization.

Figure 8 shows that for a given segment the displacement is not the same for all the W atoms. It can even occur in opposite directions for W atoms belonging to the same segment. These features show that the defect of orientation has a more complex structure than the one depicted by Fig. 10. Figure 8 shows also that the magnitude of the W displacements near the P atoms at the two extremities of a given slab is quite different: the displacement of $W1b$ near $P(b)$ is always very small while that of $W1a$ near $P(a)$ is sometimes important.

Because of the zero \mathbf{b}^* component of the modulation, the modulated structure contains WO_3 layers identical to that shown in Fig. 8 translated by \mathbf{b} . By this operation, a segment of given polarization is, in most of the cases, surrounded along \mathbf{b} by two segments where the W displacements are in the opposite direction. This leads generally to an AFE-like order along \mathbf{a} and \mathbf{b} . The modulation of two successive slabs in the \mathbf{c} direction are related by the screw axis 2_1 symmetry.

B. Comparison with the antiferroelectric structure of WO_3

In the MPTBp series, of formula $(PO_2)_4(WO_3)_{2m}$, the thickness of the WO_3 -type slabs increases with the m value.

For high values of m , it is reasonable to assume that the structure of the slabs tends to the one of WO_3 , despite the geometrical influence of the PO_4 tetrahedra located on each side of the slabs. It is thus interesting to compare the structural modulation of $P_4W_{20}O_{68}$ with those found in WO_3 . At high temperature, WO_3 undergoes an AFE displacement of the W atoms with respect to an hypothetical perovskite basis lattice.^{30,31} WO_3 shows a complex phase diagram with, in addition to the high-temperature AFE displacement of the W atoms, several antiferrodistortive transitions related to different kinds of rotations of the WO_6 octahedra.³² In the high-temperature phase, the W atoms are displaced from the center of the WO_6 octahedron towards an oxygen atom along one of the perovskite unit-cell directions. This displacement is in phase (i.e., ferroelectric) along the octahedra in this direction and out of phase (i.e., AFE) in the two perpendicular directions.

The superstructure of $P_4W_{20}O_{68}$ bears some resemblance with the AFE structure of WO_3 by (i) the ferroelectric-like displacement of the W in the segment (i.e., perovskite) direction (Fig. 9), (ii) the AFE-like order of these displacements between neighboring segments (Fig. 10).

Upon heating, the critical wave vector $\mathbf{q}_d = \frac{3}{7}\mathbf{a}^*$ of the modulation continuously evolves towards the value $\mathbf{q}_0 = \frac{1}{2}\mathbf{a}^*$.⁶ Therefore one expects, as this last wave vector leads to a doubling of the \mathbf{a} parameter, that the modulated structure of the WO_3 layers of $P_4W_{20}O_{68}$ will become, upon heating, closer to the AFE one of WO_3 . In this respect it is interesting to remark that, in a preliminary study of the modulation exhibited at RT by the large m members,⁶ it was possible to account for the distribution of intensity of the \mathbf{q}_0 superstructure spots using the AFE structure of WO_3 to model the W displacements (i.e., ferroelectric displacement of the W in the segment direction and out of phase between neighboring segments).

C. Basic structural instability

The ferroelectric-like polarization of the segment of ten WO_6 octahedra in $P_4W_{20}O_{68}$ recalls the polarization of the CDW found in the low m members of the MPTBp's. In the $m=4, 6$, and 7 members the CDW transitions are announced by an important regime of 1D structural pretransitional fluctuations located on the $\mathbf{a} \pm \mathbf{b}$ chains. They give rise to a sizeable x-ray diffuse scattering which was quantitatively analyzed in Refs. 5 and 33. The important finding of this analysis is that the main polarization of the CDW instability corresponds to a ferroelectriclike displacement of the W atoms inside each segment of m octahedra. In the incommensurate modulation it is only the amplitude of this “ferroelectric” wave which is modulated with the $2\pi/2k_F$ periodicity from one segment to the other along the chain direction. Interestingly, this study showed that the average direction of polarization makes an angle with the segment direction which decreased when m increased from 4 to 7. This result and our study for $m=10$ show that, as m increases (i.e., as the octahedra are less disturbed by the presence of the terminal PO_4 groups), the W displacements tend to align with the segment direction.

In relationship with these findings, the x-ray patterns of the MPTBp's exhibit at RT, whatever the m value, very

broad diffuse lines along about the $2\mathbf{a}^* \pm 3\mathbf{b}^*$ directions of the reciprocal space. This diffuse scattering, which occurs in a direction perpendicular to that $(3\mathbf{a} + 2\mathbf{b} - 0.25\mathbf{c})$ of the segment of m octahedra, means that each individual segment is the object of an incipient structural instability. As the structure factor of this diffuse scattering is that of the segment of m W atoms (which mostly scatter the x rays), the basic instability corresponds to an in phase (i.e., ferroelectric-like) displacement of the W atoms. The pretransitional CDW fluctuations observed in the low m members are located inside these broad diffuse lines. All these features mean that both the CDW instabilities and the AFE instability of the MPTBp's involve the same type of critical ferroelectric-like distortion of the segment of m octahedra.

D. CDW modulation of $\text{P}_4\text{W}_{20}\text{O}_{68}$

Among the MPTBp's the $m = 10$ and 11 members present a singular behavior. At the difference of the other members undergoing several phase transitions, where each transition stabilizes a different modulation, these two members exhibit only a single phase transition with a temperature-dependent modulation.⁶ The mechanism driving the structural phase transition(s) for the large m members is not known. However, let us mention that preliminary measurements of the thermal dependence of the electrical resistivity of the $m = 10$ member,¹⁹ suggest, by the observation of an anomaly at about 450 K, that the structural phase transition could be of the CDW type. In that context the CDW instability could be stabilized by a FS nesting mechanism. Indeed band-structure calculations performed in an extended Hückel model for the $m = 8$ and 12 members³⁴ indicate that \mathbf{q}_d could be a good nesting wave vector for the oblique parts of the FS of the large m members. In that case the FS nesting mechanism could be similar to that of the upper transition of the $m = 6$ member, where the nesting of the two bands associated to the chains parallel to the $\mathbf{a} \pm \mathbf{b}$ directions stabilizes the $\mathbf{q}_d = (0.385, 0, 0)$ modulation;⁵ the increase of \mathbf{q}_d when m increases being due to the emptying of the band associated to the chains running along \mathbf{a} and to the concomitant filling of the bands associated to the $\mathbf{a} \pm \mathbf{b}$ chains. The thermal variation of the modulation wave vector may be caused by the improvement of this nesting when the FS thermal broadening decreases upon cooling. It is also possible that such a thermal variation allows to nest at low temperature the quasi-1D FS associated to the chains \mathbf{a} , because with the electron conservation law,⁵

$$2k_F^a + 4k_F^d = 1,$$

its $2k_F^a$ wave vector amounts to $\frac{1}{2}\mathbf{a}^*$, which also corresponds, within a reciprocal-lattice wave vector, to the second harmonic of the primary modulation of wave vector $2k_F^d = \frac{2}{3}\mathbf{a}^*$.

It is also interesting to remark that in a batch of $m = 10$ crystals prepared in different conditions¹⁹ the modulation remains short-range ordered around the \mathbf{q}_0 critical wave vector on all the temperature range. This could be due to the stabilization of the \mathbf{q}_0 order because of an excessive broadening of the FS, possibly due to a large amount of defects in the structure. In this respect it has been shown from high-resolution electron microscope studies³⁵ that when m in-

creases the occurrence of intergrowth defects involving other members of the series increases. In that case there is a charge transfer between the layers of different m values and the number of conduction electrons does not remain exactly 2 electrons per segment of m octahedra. This leads to a spreading of the FS which is more likely its main cause of broadening. Finally, let us remark that \mathbf{q}_0 is also the modulation wave vector common to the high m members.⁶

In a general way, the thermal variation of the modulation wave vector from its \mathbf{q}_0 high-temperature value can be described by the establishment of a periodic lattice of defects inside an underlying AFE lattice. If one neglects the variation of the amplitude of the polarization, Fig. 10 shows that a defect leads to a phase shift of π between two successive AFE orders. In this picture the repeat distance between two successive defects (or the size of the regular AFE domains) will decrease upon cooling, reaching $7\mathbf{a}$ at RT. In presence of disorder such a periodic order of defects cannot be set on a long distance. In case of strong disorder, which seems to be present in the second batch of crystals, the diffraction only reveals the \mathbf{q}_0 AFE short-range order; the coherence length of the order thus corresponding to the average size of the AFE domains.

With respect to the AFE order of insulating WO_3 , the RT $7\mathbf{a}$ lattice periodicity of the phase defects of this order could be attributed to the setting of the CDW in metallic $\text{P}_4\text{W}_{20}\text{O}_{68}$; the electron being more localized in the phase defects. It is also interesting to remark that if the $\frac{3}{7}\mathbf{a}^*$ modulation, associated with the first-order satellite reflections, corresponds to the $2k_F$ critical wave vector of the 1D electron gas associated to the $\mathbf{a} \pm \mathbf{b}$ chains, the second-order satellite reflections at $\frac{1}{7}\mathbf{a}^* [= (1 - \frac{6}{7})\mathbf{a}^*]$ correspond to its $4k_F$ critical wave vector. By its wave vector this last instability recalls the \mathbf{q}_d instability which becomes the dominant one for the larger m members (i.e., when the electron density, which decreases as $2/m$, becomes smaller).

E. Coupling between the lattice and electronic degrees of freedom in the MPTBp's

The ferroelectric-like displacement of the W atoms away from their average position in the WO_6 octahedra and their AFE-like order between neighboring segments (see arrows in Fig. 8) leads to a sizeable change of the electronic parameters such as the site energy or the transfer integrals. Because of the low symmetry of the octahedra such quantities are changed at first order in lattice displacements. The change of interatomic distances which thus result leads to a modulation of the electronic density. In short this gives rise to a first-order electron-phonon coupling necessary to achieve the formation of CDW. More precisely, the ferroelectric-like displacement of the W atoms changes the relative position of the energy levels of the t_{2g} W orbitals and thus those of the segments of m octahedra on which the three sets of 1D bands running along the \mathbf{a} and $\mathbf{a} \pm \mathbf{b}$ directions are constructed.¹⁶ In addition, the AFE-like order modulates the transfer integrals of these bands. This kind of lattice displacement will provide the first-order electron-phonon coupling required to achieve the simultaneous nesting of the differently oriented 1D FS of the MPTBp's. Such a transition-metal displacement could be also present in the other oxides and bronzes built with

ReO₃-type layers, such as the purple bronze and Mo₄O₁₁, which exhibit a CDW ground state due also to a hidden nesting mechanism.^{5,16,17}

F. Secondary distortions of P₄W₂₀O₆₈

1. Monoclinic distortion and twin phenomenon

The weak monoclinic lattice distortion observed at RT in P₄W₂₀O₆₈ with **c** as the twofold axis, associated with a twin phenomenon, is not unique among the MPTBp's since it has also been observed in the modulated structure of the $m = 12$,³⁶ $m = 13$,³⁷ and $m = 14$ (Ref. 36) members. However, x-ray measurements upon heating⁶ show that, above T_c , the symmetry becomes orthorhombic and the twinning disappears. Since below T_c the AFE-type modulation is set, it is thus easy to correlate the monoclinic distortion and the lattice twinning with the occurrence of the AFE-like order. By the onset of the ferroelectric-like W displacement in a given set of segments of ten WO₆ octahedra, the **a**+**b** and **a**-**b** chain directions become no longer equivalent. This leads to a deviation from 90° for the γ angle between **a** and **b**. The decrease of γ could probably be stabilized by a better gain of nesting energy. Therefore the orthorhombic symmetry is changed into a monoclinic one with the binary axis directed along **c**. The two components of the twin are due to the two possible choices for the W ferroelectric-like displacement in the segments of ten octahedra.

2. Average ferroelectric polarization

The space group of the superstructure of P₄W₂₀O₆₈ is P2₁, with the twofold screw axis directed along **c**. The orientation symmetry of the crystal, 2, allows the establishment of a ferroelectric macroscopic polarization along the **c** direction. Figure 10 shows that, at RT, because of the 7**a** lattice periodicity and of the inequality in the W shift amplitudes, each WO₃ layer exhibits, in a direction close to the segment direction, a weak spontaneous polarization. This polarization cannot be reversed by the application of the screw axis symmetry directed along **c** when one passes from a layer to the next one. This allows the setting of a macroscopic polarization along the **c** direction. Its magnitude is, however, not known. It should be interesting to perform dielectric measurements in order to verify the onset at T_c of a spontaneous

ferroelectric polarization. Such measurements are, however, quite difficult to perform because of the metallic-like conductivity of the samples.

V. CONCLUSION

In the present work we have determined the RT CDW structure of P₄W₂₀O₆₈, the $m = 10$ member of the series of monophosphate tungsten bronzes (PO₂)₄(WO₃)_{2m}.

The modulation is mainly due to a displacement of the tungsten atoms inside the WO₆ octahedra forming the WO₃-type slabs. This feature and the large amplitude (~ 0.1 Å) of the displacement account for the high x-ray intensity of the satellite reflections observed. The anionic sublattice of tilted octahedra is apparently not disturbed by the modulation. Another important feature revealed by this structural determination is that the W displacements are mainly aligned with the average direction of a segment of ten WO₆ octahedra bounded at each end by a PO₄ tetrahedron, giving rise to a main polarization of the ferroelectric type at this segment. This and the AFE-like order between segments are probably the right lattice displacements allowing the simultaneous nesting of the differently oriented quasi-1D FS (Ref. 17) at the origin of the CDW instabilities of the ReO₃-type W and Mo oxides and bronzes.

Another important feature of the 7**a**×**b**×**c** superstructure is that the W displacements tend to alternate between neighboring segments along **a**. The presence of an AFE-like modulated order with a $2\pi/q_d$ periodicity could be the compromise found for the large m members to stabilize a CDW ground state, as in the low m members, while keeping the AFE modulation of WO₃.

During the completion of this work, an x-ray determination of the CDW modulated structure of P₄W₈O₃₂, the term $m = 4$ of this series, has been independently performed.³⁸ The crucial role of W atoms in the onset of the CDW modulation is also emphasized but compared to P₄W₂₀O₆₈, the W displacements are very weak and differently oriented. The weakness of the W displacements can be accounted by the large difference of T_c between the $m = 4$ and $m = 10$ members (80 K versus 450 K). The different orientation of the displacement can be understood by the irrelevance of the AFE instability of WO₃ in such a low m member.

*Electronic address: pascal.roussel@ismra.fr

¹B. Raveau, C. Michel, M. Hervieu, and D. Groult, *Crystal Chemistry of High T_c Copper Oxides*, Springer Series in Material Science Vol. 15 (Springer Verlag, Berlin, 1991).

²*Colossal Magnetoresistance and Related Properties of Manganese Oxides*, edited by C. N. R. Rao and B. Raveau (World Scientific, Singapore, 1998).

³Y. Ueda, *Chem. Mater.* **10**, 2653 (1998).

⁴*Oxide Bronzes*, edited by M. Greenblatt, *Int. J. Mod. Phys. B* **7**, 23 (1993); *Physics and Chemistry of Low Dimensional Inorganic Conductors*, Vol. 354 of *NATO Advanced Study Institute, Series B: Physics*, edited by C. Schlenker, J. Dumas, M. Greenblatt, and S. van Smaalen (Plenum, New York, 1996).

⁵P. Foury and J. P. Pouget, *Int. J. Mod. Phys. B* **7**, 3973 (1993).

⁶A. Ottolenghi and J. P. Pouget, *J. Phys. I* **6**, 1059 (1996).

⁷C. Schlenker, C. Hess, C. Le Touze, and J. Dumas, *J. Phys. I* **6**, 2061 (1996).

⁸S. L. Wang, C. C. Wang, and K. H. Lii, *J. Solid State Chem.* **82**, 298 (1989).

⁹J. P. Giroult, M. Goreaud, Ph. Labbé, and B. Raveau, *Acta Crystallogr., Sect. B: Struct. Crystallogr. Cryst. Chem.* **37**, 2139 (1981).

¹⁰A. Benmoussa, Ph. Labbé, D. Groult, and B. Raveau, *J. Solid State Chem.* **44**, 318 (1982).

¹¹P. Roussel, P. Foury-Leylekian, B. Domengès, D. Groult, Ph. Labbé, and J. P. Pouget, *Eur. J. Phys. B* **12**, 497 (1999).

¹²Ph. Labbé, M. Goreaud, and B. Raveau, *J. Solid State Chem.* **61**, 324 (1986).

¹³P. Roussel, Ph. Labbé, D. Groult, B. Domengès, H. Leligny, and D. Grebille, *J. Solid State Chem.* **122**, 281 (1996).

- ¹⁴P. Roussel, G. Mather, B. Domengès, D. Groult, and Ph. Labbé, *Acta Crystallogr., Sect. B: Struct. Sci.* **54**, 365 (1998).
- ¹⁵P. Roussel, D. Groult, A. Maignan, and Ph. Labbé, *Chem. Mater.* **11**, 249 (1999).
- ¹⁶E. Canadell and M. H. Whangbo, *Phys. Rev. B* **43**, 1894 (1991).
- ¹⁷M. M. Whangbo, E. Canadell, P. Foury, and J. P. Pouget, *Science* **252**, 96 (1991).
- ¹⁸A. Ottolenghi, P. Foury, J. P. Pouget, Z. S. Teweldemedhin, M. Greenblatt, D. Groult, J. Marcus, and C. Schlenker, *Synth. Met.* **70**, 1301 (1995).
- ¹⁹C. Schlenker, C. Le Touze, C. Hess, A. Rötger, J. Dumas, J. Marcus, M. Greenblatt, Z. S. Teweldemedhin, A. Ottolenghi, P. Foury, and J. P. Pouget, *Synth. Met.* **70**, 1263 (1995).
- ²⁰H. Böhm, *Acta Crystallogr., Sect. A: Cryst. Phys., Diffr., Theor. Gen. Crystallogr.* **31**, 622 (1975).
- ²¹B. Doudin (private communication).
- ²²W. R. Busing and H. A. Levy, *Acta Crystallogr.* **10**, 180 (1957).
- ²³V. Petricek and M. Dusek, JANA98, Institute of Physics, Praha, Czech Republic, 1997.
- ²⁴S. van Smaalen, *Acta Crystallogr., Sect. A: Found. Crystallogr.* **A43**, 202 (1987).
- ²⁵P. M. de Wolff, T. Jansen, and A. Janner, *Acta Crystallogr., Sect. A: Cryst. Phys., Diffr., Theor. Gen. Crystallogr.* **A37**, 625 (1981).
- ²⁶B. Dam and A. Janner, *Acta Crystallogr., Sect. B: Struct. Sci.* **B42**, 69 (1986).
- ²⁷W. Steurer, *Acta Crystallogr., Sect. A: Found. Crystallogr.* **A43**, 36 (1987).
- ²⁸A. Frost-Jensen, F. Krebs Larsen, B. Brummerstedt Iversen, V. Petricek, T. Schultz, and Y. Gao, *Acta Crystallogr., Sect. B: Struct. Sci.* **B53**, 113 (1997).
- ²⁹D. Watkin, *Acta Crystallogr., Sect. A: Found. Crystallogr.* **A50**, 411 (1994).
- ³⁰W. L. Kehl, R. G. Hay, and D. Wahl, *J. Appl. Phys.* **23**, 212 (1952).
- ³¹T. Vogt, M. Woodward, and B. A. Hunter, *J. Solid State Chem.* **144**, 209 (1999).
- ³²Ph. Labbé, in *Diffusionless Phase Transitions and Related Structures in Oxides*, edited by C. Boulesteix (Trans Tech Publications, Zurich, Switzerland, 1992), pp. 293–339.
- ³³P. Foury, J.-P. Pouget, Z. S. Teweldemedhin, E. Wang, M. Greenblatt, and D. Groult, *J. Phys. IV* **3**, C2 133 (1993).
- ³⁴E. Canadell (unpublished).
- ³⁵B. Domengès, M. Hervieu, B. Raveau, and R. J. D. Tilley, *J. Solid State Chem.* **54**, 10 (1984).
- ³⁶P. Roussel, Ph. Labbé, and D. Groult (unpublished).
- ³⁷V. Favre-Nicolin and J. L. Hodeau (private communication).
- ³⁸J. Ludecke, A. Jobst, and S. van Smaalen, *Europhys. Lett.* **49**, 357 (2000).